Progress in microscopic modeling of damage in steel at high temperature

Marc REMY, Sylvie CASTAGNE, Anne Marie HABRAKEN

Institute of Mechanics & Civil Engineering
University of Liège
M&S Department
chemin des Chevreuils, 1
B-4000 Liège 1
Belgium

Anne.Habraken@ulg.ac.be

ABSTRACT. *With the goal to study crack propagation in continuous casting, this paper presents an on going project to develop and identify a mathematical finite element model of damage in steel at high temperature. A representative microscopic cell of the material is presented and adapted to available chemical information, precipitation state and micro-structures observed using metallographic as well as imaging methods (optical microscopy, SEM, orientation imaging microscopy). Compression tests of cylindrical samples after a thermal treatment have been performed to identify the parameters of an elasto-visco-plastic law of Norton-Hoff type. Hot damage tests in tensile and compression states help to provide information on crack appearance.*

RÉSUMÉ. *Avec pour finalité l'étude de la propagation de fissures lors de la coulée continue de l'acier, nous présentons une recherche en cours pour développer et calibrer un modèle par éléments finis de l'endommagement de l'acier à haute température. Une cellule microscopique représentative du matériau est introduite et adaptée à l'information chimique disponible, à l'état de précipitation, et aux microstructures observées tant par des méthodes métallographiques que par des méthodes d'imagerie (microscopie optique, SEM, microscopie à orientation d'images). Des essais de compression d'échantillons cylindriques après traitement thermique ont été réalisés afin de calibrer les paramètres d'une loi élasto-visco-plastique de type Norton-Hoff. Des essais de compression et de traction à chaud ont contribué à fournir les informations sur l'apparition de la fissure.*

KEYWORDS: *elasto-visco-plastic constitutive law, steel, austenite, damage*

MOTS-CLÉS : *loi constitutive élasto-visco-plastique, acier, austénite, endommagement*

1. Introduction

This research, performed in collaboration with industrial partners of the ARCELOR group (IRSID and the Technical Direction of Cockerill Sambre), aims to study steel at high temperature. A damage model using a numerical microscopic[1] approach is identified by experimental measurements obtained from the microscopic and macroscopic scales. The final goal is a parametrical study of various microscopic factors such as grain size or precipitation state in continuous casting process.

Constitutive laws have been implemented into a finite element code. They are applied to study the initiation and propagation of cracks in the industrial process of continuous casting. A macroscopic finite element study of this process (see [PAS 00]) provides global stress and strain fields defining the loading of the microscopic cell during the process.

For the studied low carbon steel, transverse cracking is recognized as a major problem in this process. Hot tensile tests have demonstrated that steel is more brittle in the temperature range from 1000°C to 600°C . The allotropic austenite/ferrite phase transformation occurs in this temperature range. This loss of ductility is responsible for the appearance of cracks during the bending and unbending operations of the strand. Other researches (see [GAM 01]) also tend to demonstrate that austenitic grain boundary is a favorable place for cracks to begin. They appear by strain concentration and micro-void coalescence at grain boundaries and by grain boundary sliding. The influence of creep, controlled by diffusion, is important in the studied temperature range. Castagne [CAS 01] proposes a literature review on this topic.

The first step in the development of the mathematical model is the building of a representative microscopic cell of the material. Diffusion of voids at grain boundary and sliding are introduced in the model.

To compare the results of a given macroscopic test with the simulation, the cell will always be submitted to stress and strain fields determined by the corresponding macroscopic experiments. Hence, we want to identify the microscopic damage law with help of finite element at microscopic scale where the applied loading is the macroscopic one.

As the micro-structure influences damage and creep, it has to be introduced if we want to determine the sensibility factors for crack initiation. The microscopic cell consists of grains and grain boundaries, as shown in Figure 1. Three essential features require identification:

– the grain size and shape,

– the constitutive law inside the grain,

– the constitutive laws defining the grain boundary behavior: sliding, pressure, cohesion ...

1. Throughout this article "microscopic" must be understood as "comparable in size with austenic grains".

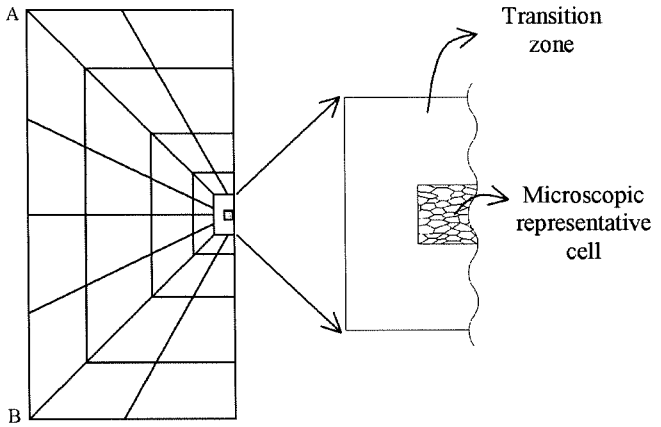

Figure 1. *Macroscopic section of the slab on which the thermo-mechanical state is computed by a macroscopic model (left picture). Microscopic cell (right picture) on which the loading from the macroscopic model will be applied.*

Metallographic and texture analysis combining optical microscopy (OM), scanning electron microscopy (SEM) and orientation image microscopy (OIM), as well as various chemical etching and visual observation on steel samples, have been performed at room temperature. These efforts to determine the previous austenitic grain size and morphology are presented. Hence the geometry of the microscopic cell is defined taking into account the results of this micro-graphic study.

The cell discretization is obtained either by automatic meshing of observed grains by OIM (with the help of a homemade dedicated software) or on purely geometrical meshes (hexagon, square, ...) whose grain sizes correspond to the observations.

A law of Norton-Hoff type has been used to quantify the visco-plastic behavior inside the grain for the studied steel. Its parameters have been identified using experimental results (see [WOL 01]). Compression tests of cylindrical samples, after a thermal treatment aiming to reproduce the thermal cycle in continuous casting have been performed. Various strain rates and temperatures have been tested and compared with simulations in order to identify this mechanical law.

Kopp et al. [KOP 99] has transposed the forming limit diagrams used in deep drawing of sheets to forging processes. Different geometries of samples are compressed at various temperature and velocity to detect a forging limit. So crack appearance depending on temperature, strain rate and strain level is identified thanks to acoustic detection during the tests. FEM simulations are then required to define forging limits with accuracy. Such a set of experiments has been applied to the studied steel to identify the constitutive law used at grain boundaries.

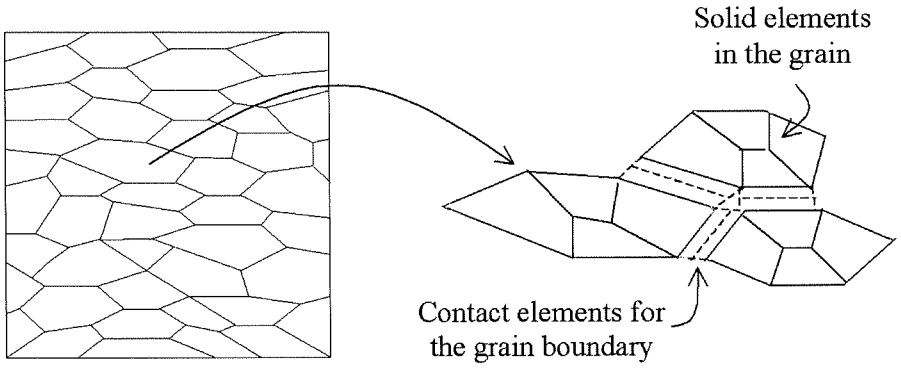

Figure 2. *Microscopic cell with solid and interface elements.*

This paper is subdivided in the following sections. Section 2 describes the microscopic cell. Section 3 explains the efforts to get information on the austenitic grain. Section 4 describes the elasto-visco-plastic law used at high temperature and summarizes its identification method. The interface finite elements and the interface law are described in Section 5 and 6 respectively. As a first application, encouraging results of crack propagation with a simple model are presented in Section 7.

2. Microscopic cell

In order to represent inter-granular creep fracture, the developed model contains solid finite elements for the grains and interface elements for their boundaries (see also [ONC 99]). The laws governing our model are described respectively in Section 4 and 6. In the grains an elasto-visco-plastic law without damage is used, and at the boundaries a law with damage is preferred. The relevant damage mechanisms at the micro-scale are viscous grain boundary sliding, nucleation, growth and coalescence of cavities leading to micro-cracks. The linking-up process subsequently leads to the formation of a macroscopic crack.

2.1. *Solid finite elements and grain representation*

The grains are modeled by thermo-mechanical 4-nodes quadrilateral solid elements BLZ2T of mixed type [ZHU 95]. Figure 2 shows a sketch of the microscopic representative cell. On the right part, a zoom on three grains allows to visualize the meshing of these grains and their interfaces.

The number of grains in the microscopic cell as well as the density of the mesh inside the grains have to be tested to define a cell which gives accurate results within an acceptable computing time.

The shape and size of grains have to be determined from the results of the microscopic analysis (see section 3).

3. Micro-structure of the studied steels

Two grades of low carbon steels (A and B), provided by the industrial partners, have been studied (see [CAS 01]). Visible surface cracks are observed on the slab corresponding to steel A.

Microscopical studies have been performed on samples extracted near one corner of the slabs, using optical microscopy, scanning electron microscopy and orientation image microscopy. Of course, these observations at room temperature detect the microstrucuture of ferrite and not austenite. Indeed, austenite exists only in a temperature range with lower and upper limits of approximately 800°C and 1100°C. As we will see in this section, observations of micro-structures at room temperature can give a reasonable idea of the austenite grain size and of its morphology at high temperature.

3.1. *From austenite to ferrite*

During the allotropic phase transformation, each austenitic grain can give birth to many ferritic grains, depending on the number of nucleation sites of ferrite, which growth successfully inside the austenite, as temperature drops. The cooling rate is the key macroscopic parameter which controls this number of ferritic grains ; a larger cooling rate implies a larger number of ferritic grains and ferritic grains of smaller size. Decrease of the ferritic grain size tends to improve the mechanical properties of the steel. In the most usual case which leads to a micro-structure of ferrite/pearlite, nucleation of ferrite starts at the boundary of austenitic grains (see Figure 3, top).

3.2. *Optical microscopy*

From the microscopical optical investigations it appears that the two studied steels present very different micro structures of ferrite near the surface: quite regular ferrite and pearlite in the case of steel A, and more complex structures, among which widmanstättite embedded in ferrite/pearlite in the case of steel B.

Widmanstättite is the micro-structure which is formed when the precipitation of ferrite grains starts inside the crystal of austenite. Micro-crystals of ferrite are oriented along the directions of the previous austenitic micro-crystal. The micro-structure is also called acidular ("needle-like") (see [COH 95] and Figure 3, bottom).

Among these complex structures of sample B, embedded in ferrite/pearlite, we have identified 3 large widmanstättite structures (typical size of 3 mm) near the slab surface in a section of 1.5 cm x 1.0 cm perpendicular to the transverse direction of the slab. The probable origin of this widmanstätten structure is a fast cooling of the

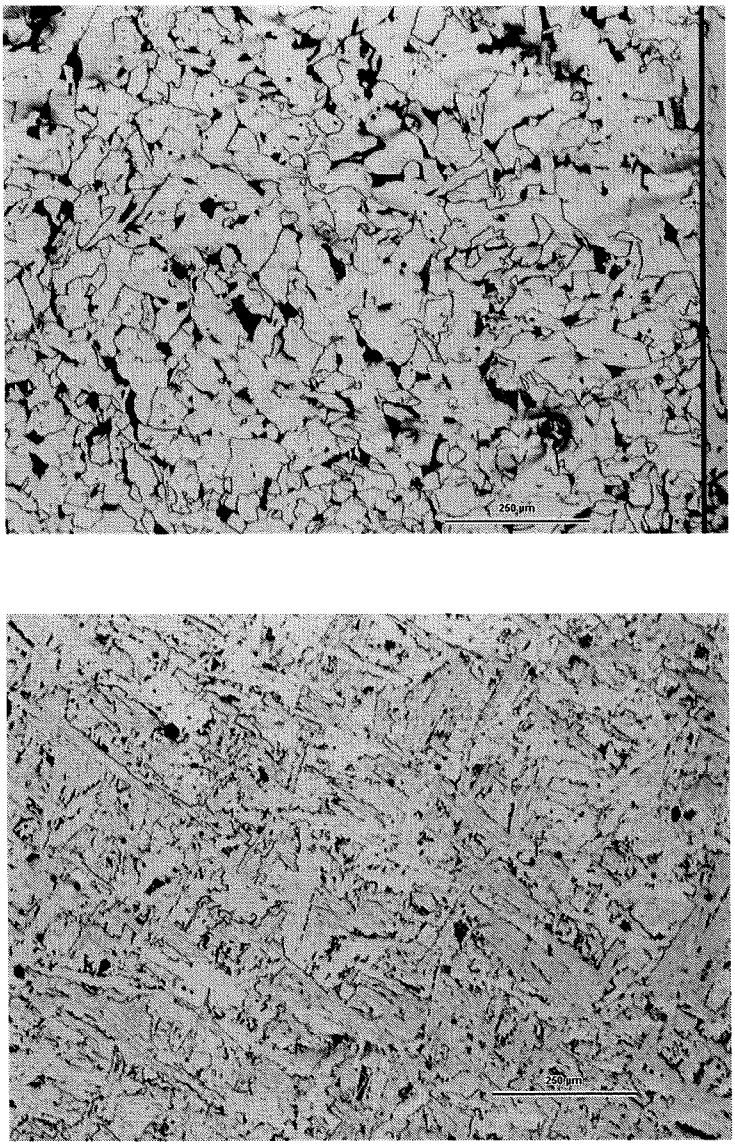

Figure 3. *Ferrite/pearlite in steel A (top) and probable widmanstättite in steel B (bottom). OIM taken inside the displayed zone of steel B indicates a common orientation for the micro-crystals of ferrite. Rolling direction of the slab is horizontal and normal direction vertical.*

slab. This hypothesis seems to be confirmed by the observation of small ferrite/pearlite grains in the first mm near the surface (not displayed).

The identification of 3 distinct widmanstättite zones result from the following observations: 1) inside each zone, elongated structures are parallel and acidular and 2) a clear texture is observed by OIM near the center of one zone (see next section, where more details are given). This implies a common micro-orientation for each zone. From this we deduce that these 3 zones are originated from 3 distinct austenitic grains. According to these considerations, the size of the austenitic grains in sample B would be of the order of 3 mm.

3.3. *Orientation imaging microscopy*

The sample preparation consists in several mechanical polishing steps then a final electro-polishing step. For this analysis, etching was done with nitric acid and stopped by methanol.

The concepts of texture of materials, orientation distributions function (ODF) and related topics are fully described in [BUN 82]).

The orientation image microscopy is a technique coupled with SEM aiming at a precise measurement of the three-dimensional orientation of micro-crystal lattice at many regularly spaced positions in the plane of the sample. This technique creates a rectangular map of the lattice orientations (Euler angles) of the grains in the sample. Each position is also called a "scan", with reference to the electron beam of the microscope. Post-processing technique of those images could include the reconstruction of grain based on the orientation of the scanned positions, pole figures, orientation distribution function, etc.

Two images with different resolutions have been obtained for steel A in the central region of the sample. These images are typical of regular ferrite grains. Measurements were quite easy with this sample, the post-processing software (see below) rates the measurements as of very high quality.

Four images with different resolutions and positions have been obtained of one of the 3 observed widmanstättite zones. The first two ones, of regular quality, were taken in the central part of the zone, the last ones, of excellent quality, in the interface between this zone and the embedding ferrite/pearlite. For the two first images of this sample, post-processing and further image analysis of measurements were necessary to make the grains appears clearly.

3.3.1. *The post-processing analysis software*

From the measurements stored in a file, a dedicated software "TSL" allows to construct pole figures and texture maps (orientation distribution functions) and a pseudo-color image of the observed sample. This software groups scans together into grains, on the basis of the observed Euler Angles of all the scans. It takes into account the

symmetry group of the studied phase in its regrouping computation. A more sophisticated treatment to regroup scans of ferrite on the basis of a common austenite origin is not possible at this stage.

As a conclusion to this study, texture was detected only for the observed zone of widmanstättite. The result for this sample is that a dominant orientation appears clearly in its center. Nevertheless, this texture does not appear near the boundary of the same zone.

3.3.2. *OIMesh*

Dedicated software "OIMesh" has been developed by our team to achieve a regrouping of ferrite grains of common austenitic origin [REM 01]. It uses similar techniques than the commercial post-processing software "TSL". Nevertheless, it is far less comprehensive but generates a format directly usable by TSL.

In the context of our austenite grain "quest", what has been tested with OIMesh is very simple. We have assumed that in the austenite to ferrite phase transformation, all the austenite atoms have a movement parallel to the crystal principal axes. (ie. the strain principal directions coincide with crystal lattice axis).

This kind of "minimal" movement is what is expected if widmanstättite is formed and nucleation of ferrite started inside the austenitic grain. As in the transformation, one of the axes is stretched and the others shrink. One can easily see that a given austenite grain gives three classes of possible ferrite grain. Each class is achieved when the corresponding axis (out of 3) becomes the stretching axis.

It can be shown with this hypothesis in mind that two given ferrite crystals coming from the same austenite grain will be rotated by multiple of 90°, the axis of rotation being a line joining the centers of two opposite edges of the bcc lattice. This hypothesis has been introduced in the algorithm of grain regrouping of OIMesh.

Processing of the 4 images obtained by OIM for steel B with help of OIMesh does not result in any significant regrouping of ferrite grains, but for some very marginal low quality measurements. Despite this rather deceiving result, modification of the detection algorithm or application to other cases could possibly lead to better results.

Let us add that, after grain regrouping, OIMesh simplifies grain boundaries keeping triple points and some supplementary points (to match more closely large boundaries between two grains) and allows the automatic meshing of the grains. It could also be used as preprocessor of a FE analysis software.

3.4. *Metallographic analysis*

Picral an nital tests have also been performed on the sample of steel B to try to enhance the austenitic boundary. Using this technique, metallographists from industry

were able to directly detect some part of the austenitic boundary by direct observation of the sample. These findings confirm the large value for the austenitic grain size.

With micro-structures as large as several mm at high temperature, one could possibly question the validity of continuous mechanics and of any isotropy or homogeneity hypothesis which could be made without taking care of the size of studied structures. This justifies the idea of using a representative cell in which the grains are modeled individually to study crack initiation and propagation.

4. Norton-Hoff constitutive law

An isotropic model for the constitutive elasto-visco-plastic law inside the grain is used. This approximation is reasonable at the current stage of our study and could easily be replaced using an anisotropic law, if necessary.

The creep behavior inside the grain can be represented by an elasto-visco-plastic law of Norton-Hoff type, Equation 1. Its parameters (p_1, p_2, p_3, p_4) have been identified thanks to the macroscopic experiments described below.

The Norton-Hoff law gives us the visco-plastic limit as:

$$\sigma_e = e^{-p_1 \varepsilon_e} \sqrt{3}\, p_2 \left(\sqrt{3}\dot{\varepsilon}_e\right)^{p_3} \varepsilon_e^{p_4} \quad , \qquad [1]$$

expressed in term of von Mises equivalent stress σ_e , strain rate $\dot{\varepsilon}_e$ and strain ε_e.

4.1. *Compression tests*

Based on experimental data (stress σ vs. strain ε) obtained for the steel B by the IBF Aachen at different strain rates $\dot{\varepsilon}$ ($0.0001\ s^{-1}$, $0.001\ s^{-1}$, $0.01\ s^{-1}$) and temperatures T (800°C, 900°C, 1000°C, 1100°C), we have determined the parameters of the Norton-Hoff law as a function of temperature by 2 different methods, independently at each temperature.

In the first method, at a given T, (p_1, p_2, p_4) are determined on the curve with $\dot{\varepsilon} = 0.001\ s^{-1}$ alone and for p_3, all the curves at this T are used. In the second method, at a given T, the 4 parameters are fitted simultaneously with all the curves at this T. Comparison of the 2 sets of parameters gives us an idea of the reliability of the identification. Plots of the parameters vs. temperature are presented in Figures 5 to 8.

As an example, Figure 4 shows how the Norton-Hoff law, after final fitting, matches the experimental points.

It results from this comparison that the parameter $p_3 \approx 0.14$ is very well identified and almost independent of the temperature. This is not the case for p_4 and p_2 which appear well determined but depend on temperature ; the relation being nearly linear for parameter p_2. The parameter p_1 is poorly determined, especially at temperature 1000°C.

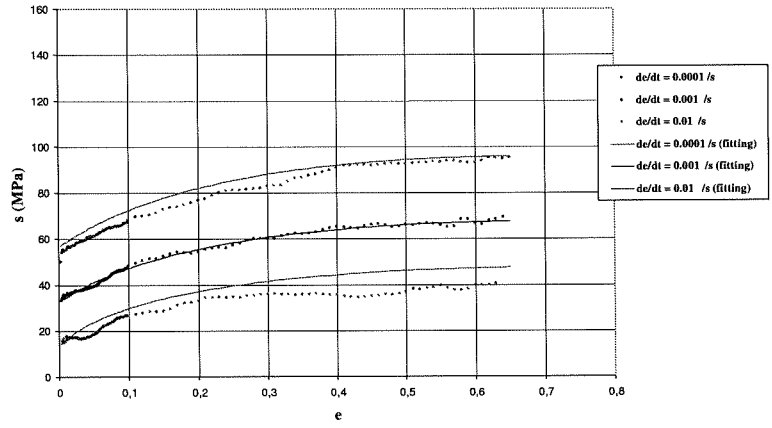

Figure 4. *Equivalent stress versus equivalent strain. An example (T=900° C) of the final χ^2-fitting of the Norton-Hoff law to the experimental points (first method described in text).*

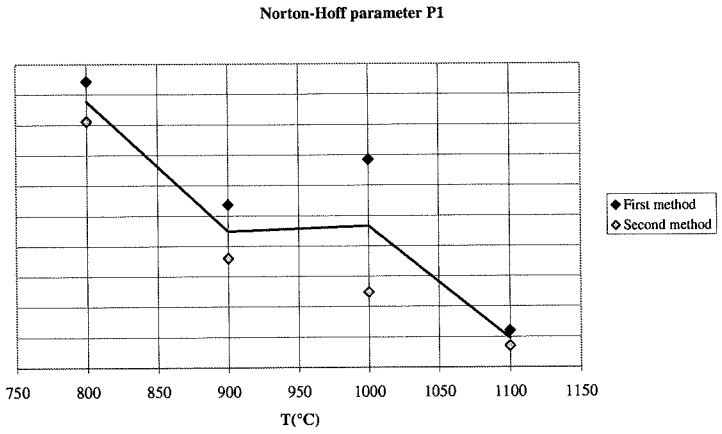

Figure 5. *Norton-Hoff parameter p_1 as a function of temperature. The linear interpolation between the mean value is also drawn.*

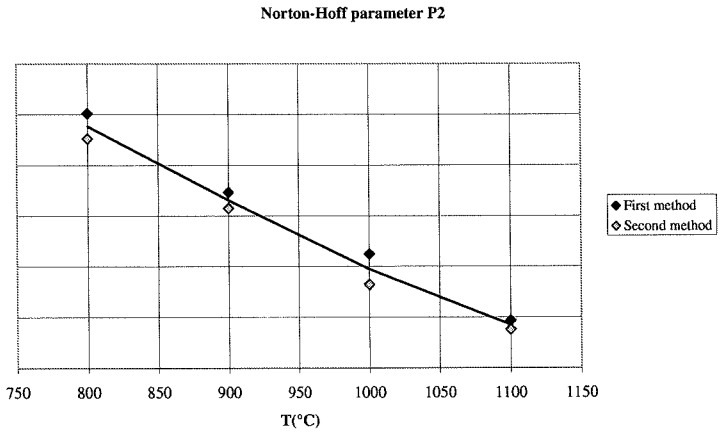

Figure 6. *Norton-Hoff parameter p_2 as a function of temperature. The linear interpolation between the mean value is drawn.*

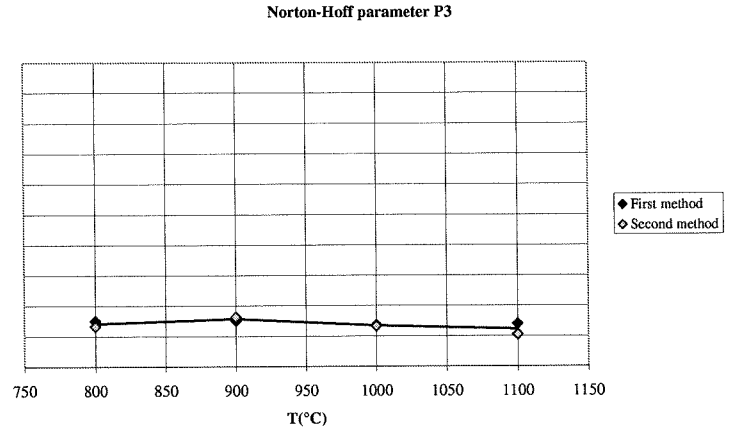

Figure 7. *Norton-Hoff parameter p_3 as a function of temperature. The linear interpolation between the mean value is drawn.*

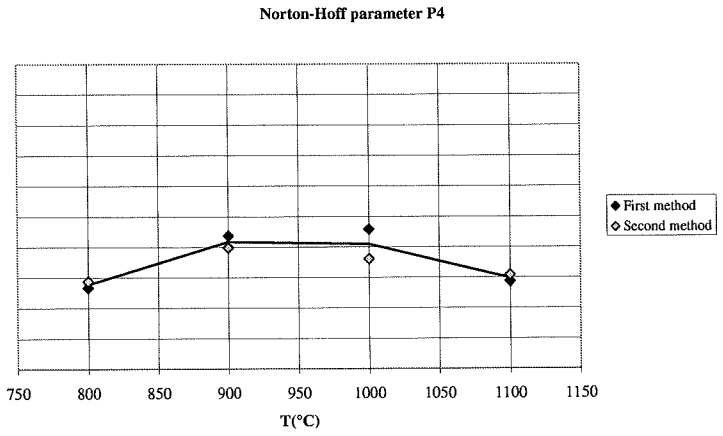

Figure 8. *Norton-Hoff parameters p_4 as a function of temperature. The linear interpolation between the mean value is drawn.*

5. Interface finite elements and grain boundary representation

The solid elements modeling the grains are connected by interface elements to account for cavitation and sliding at the grain boundary (see [ONC 99]). As the thickness of the grain boundary is small compared to the grain size, the grain boundary is represented by one-dimensional interface elements. These elements are associated with a constitutive law which includes parameters linked to the presence of precipitates, voids, etc (see Section. 6). The damage variable explicitly appears in this law.

The interface element is composed of a modified contact element and a foundation element (see Figure 9).

For each integration point of the contact element, the program determines the associated foundation segment as well as the solid element to which the foundation is associated. The state variables for the interface element are computed using information of the two solids elements in contact (elements i and j in Figure 9). The state variables in the interface element are the algebraic average of the corresponding values at the integration points of elements i and j. This is obviously a rough approximation. Better schemes will be tested in the near future.

The original contact element is described in [HAB 98] and is usually combined with a Coulomb friction law. This element has been modified in order to introduce a

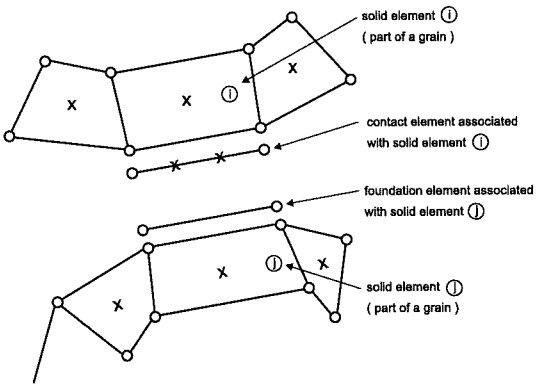

Figure 9. *Interface element: contact element,associated foundation, linked solid elements. The dots symbolize nodes and the crosses represent integration points. For clarity, a gap has between introduced between the contact element and the associated solid element, as also between the foundation and the solid element.*

new interface law and a cohesion criterion. The behavior of the interface element is described by the following eleastic-type relationships:

$$\dot{\tau} = k_{\mathrm{s}}(\dot{u} - \dot{u}_{\mathrm{s}}) \quad \text{and} \quad \dot{\sigma}_s = k_{\mathrm{n}}(\dot{\delta} - \dot{\delta}_{\mathrm{s}}) \quad , \qquad [2]$$

where $\dot{u}$ and $\dot{\delta}$ are the unknown relative velocities of adjacent grains due to shear stress τ (respectively parallel and normal to the grain boundary). This is a penalty method where the coefficients k_{s} and k_{n} are very large to keep the deviations $(\dot{u} - \dot{u}_{\mathrm{s}})$ and $(\dot{\delta} - \dot{\delta}_{\mathrm{s}})$ small. The evolution of $\dot{u}_{\mathrm{s}}$ (see Equation 3) and of $\dot{\delta}_{\mathrm{s}}$ (see Equation 13) will be computed in the next section.

The interface element is supposed to be in contact with the foundation (i.e. no crack) until a damage variable defined by the ratio a/b (see next sections) reaches a threshold value.

6. Interface law

6.1. *Evolution of the damage variable*

6.1.1. *Grain boundary sliding*

According to Ashby [ASH 72], grain boundary sliding is governed by:

$$\dot{u}_{\mathrm{s}} = w\frac{\tau}{\eta_{\mathrm{B}}} \quad , \qquad [3]$$

where $\dot{u}_s$ is the relative velocity between two adjacent grains, w is the thickness of the grain boundary and η_B is the grain boundary viscosity. However in [ONC 99], η_B/w is expressed in term of the strain-rate parameter $\dot{\varepsilon}_B$ defined as follows:

$$\dot{\varepsilon}_B = \dot{\varepsilon}_o \left(\frac{w\sigma_o}{\eta_B \dot{\varepsilon}_o d} \right)^{\frac{n}{n-1}} \quad , \qquad [4]$$

with d a length parameter related to the grain size, n the creep exponent. σ_o, $\dot{\varepsilon}_o$ are reference stress and strain-rate.

6.1.2. *Grain boundary cavitation*

In the context of damage at high temperature, the mechanism of voids nucleation, growth and coalescence is established.

6.1.2.1. Nucleation

In most engineering alloys, cavities have been observed to nucleate continuously. The following experimental relation has been suggested [GIE 94]:

$$\dot{N} = \beta \sigma_n^2 \dot{\varepsilon}_e^C = F_n \left(\frac{\sigma_n}{\Sigma_o} \right)^2 \dot{\varepsilon}_e^C \quad \text{with} \quad \sigma_n \geq 0 \quad , \qquad [5]$$

where N is the average number of cavities per unit length of grain boundary,$\dot{\varepsilon}_e^C$ is the effective creep strain rate, σ_n the normal stress, introduced to allow a faster nucleation on those grain boundaries which are perpendicular to the loading direction, and β a material constant.

For the second formulation, F_n is the nucleation parameter of the material and Σ_o a normalization constant. F_n is the micro-structural parameter which influences the nucleation rate at the grain boundary. Through this parameter, we can introduce zones where the nucleation is more important, to take into account the precipitation state for instance.

According to Equation 5, the nucleation will begin with the plastification. Experimentally, nucleation appears sometimes later, that is why we have to introduce a threshold to indicate the beginning of the nucleation. We define the parameter S which combines the stress and the cumulated strain:

$$S = \left(\frac{\sigma_n}{\Sigma_o} \right)^2 \varepsilon_e^C \quad . \qquad [6]$$

This parameter S characterizes the state of the material before nucleation. It will grow with the strain and when the threshold value is reached, nucleation begins and the parameter S has no more utility. To define the threshold value S_{thr}, we suppose that it is related to a minimum cavity density N_I from which nucleation can be observed and a factor F_n indicating the importance of the nucleation activity of the material:

$$S_{thr} = \frac{N_I}{F_n} \quad . \qquad [7]$$

Finally, experience shows that the cavity density tends to saturate for large creep strains, thus we will suppose that nucleation of new cavities stops when N reaches the value $N_{\max}$.

If $2b$ is the cavity spacing, N is related to it by $N = 1/(\pi b^2)$. We have:

$$\dot{b} = -\frac{1}{2}\frac{\dot{N}}{N}b = -\frac{\pi}{2}b^3\beta\sigma_{\mathrm{n}}^2\dot{\varepsilon}_{\mathrm{e}}^{\mathrm{C}} \quad . \qquad [8]$$

The nucleation rate $\dot{N}$ is related to the internal state of the material N as well as to the stress σ_{n} and strain rate $\dot{\varepsilon}_{\mathrm{e}}^{\mathrm{C}}$ states on the grain boundary. With a one-dimensional element, this nucleation rate $\dot{N}$ can be interpreted as a measure of the rate of evolution of the cavity spacing $\dot{b}$.

This equation can be used to compute the decrease rate of b due to continuous nucleation of cavities.

6.1.2.2. Void growth

A detailed formulation of the cavity growth under diffusion and creep deformations can be found in [TVE 84]. A summary is proposed in Liu et al. [LIU 94] and reported hereafter. An idealized formulation of the grain boundary geometry is used: the cavities are supposed to be uniformly distributed with an average spacing of $2b$ and a diameter of $2a$. For the proposed idealized boundary geometry with a cavity tip angle $2\Psi \approx 75°$, the cavity growth rate is:

$$\dot{a} = \frac{\dot{V}}{4\pi a^2 h(\Psi)} = \frac{\dot{V}_1 + \dot{V}_2}{4\pi a^2 h(\Psi)} \quad , \qquad [9]$$

where $h(\Psi) = [(1+\cos(\Psi))^{-1} - 0.5\cos(\Psi)]/\sin(\Psi)$ (shape function of the cavity) and $\dot{V}$ is the total cavity volume growth rate, which is divided into diffusion growth part $\dot{V}_1$ and creep deformation part $\dot{V}_2$:

$$\dot{V}_1 = 4\pi D\frac{\sigma_{\mathrm{n}}}{\ln(1/f) - (3-f)(1-f)/2} \quad , \qquad [10]$$

and

$$\dot{V}_2 = \begin{cases} -2\pi\dot{\varepsilon}_{\mathrm{e}}^{\mathrm{C}}a^3h(\Psi)\left(\dfrac{3}{2n}\left|\dfrac{\sigma_{\mathrm{m}}}{\sigma_{\mathrm{e}}}\right| + \dfrac{(n-1)(n+0.4319)}{n^2}\right)^n & \text{for} \quad \dfrac{\sigma_{\mathrm{m}}}{\sigma_{\mathrm{e}}} < -1 \\ 2\pi\dot{\varepsilon}_{\mathrm{e}}^{\mathrm{C}}a^3h(\Psi)\left(\dfrac{3}{2n} + \dfrac{(n-1)(n+0.4319)}{n^2}\right)^n & \text{for} \quad \left|\dfrac{\sigma_{\mathrm{m}}}{\sigma_{\mathrm{e}}}\right| \le 1 \\ 2\pi\dot{\varepsilon}_{\mathrm{e}}^{\mathrm{C}}a^3h(\Psi)\left(\dfrac{3}{2n}\dfrac{\sigma_{\mathrm{m}}}{\sigma_{\mathrm{e}}} + \dfrac{(n-1)(n+0.4319)}{n^2}\right)^n & \text{for} \quad \dfrac{\sigma_{\mathrm{m}}}{\sigma_{\mathrm{e}}} > 1 \end{cases} \quad , \qquad [11]$$

where D is a constant related to the material diffusion, n the creep exponent, σ_n, σ_e, and σ_m are respectively the normal, effective, and mean stresses applied to the grain boundary.

The variable f is defined as follows:

$$f = \max\left\{\left(\frac{a}{b}\right)^2, \left[\frac{a}{a+1.5L}\right]^2\right\} \quad \text{where} \quad L = \left(D\frac{\sigma_e}{\dot{\varepsilon}_e^C}\right)^{1/3} \quad . \qquad [12]$$

The coupling between diffusive and creep contribution to void growth is introduced trough the length scale L: for small values of a/L, cavity growth is dominated by diffusion while for larger values, creep growth becomes more and more important.

Finally the discrete cavity distribution is replaced by a continuous distribution on each facet of the grain boundary so that the cavity volume V and the average separation between two grains δ_C evolve in a continuous way on the facet. Then, the separation rate is given by:

$$\dot{\delta}_C = \frac{\dot{V}}{\pi b^2} - \frac{2V}{\pi b^2}\frac{\dot{b}}{b} \quad . \qquad [13]$$

6.1.2.3. Void coalescence

The coalescence takes place when cavities are sufficiently close to each other to collapse. At this moment, the crack begins to propagate and the interface elements are no more in contact.

For Onck [ONC 99], the parameter used to define the coalescence activation is the ratio a/b. We call it a damage variable in our model. When this ratio reaches the value 0.7, coalescence is triggered and crack appears.

6.2. *Identification of damage parameters*

The goal of the acoustic tests is to provide a set of experiments to identify the parameters of the interface law (grain boundary behavior). At the origin, they were developed at IBF in Aachen to predict the formability of metals at low temperature and were then adapted to the conditions prevalent during hot forming. This is the same concept as the forming limit diagram used in metal sheets but here for massive samples.

During forming, when the internal stresses at a material point exceed locally a stress limit, there is a sudden microscopic crack. This new state of equilibrium has a lower potential energy. The potential energy emitted in this way is dissipated in form of elastic waves and can be detected as sound pulses. Piezoelectric sensors are used to record these sound signals. The weak sound signal is pre-amplified, filtered to separate process-relevant and interfering signals and amplified again before to be stored into to data acquisition of the computer.

The samples were first heated to 1375°C in a radiation furnace. To protect the sample material against surface oxidation, the furnace was rinsed with argon inert gas. Afterwards the samples were put in the compression device. The surrounding furnace was heated up to test temperature within an argon inert gas atmosphere. Finally, the samples were compressed with a constant strain rate up to crack initiation, while upcoming acoustic emission events caused by material failure were recorded.

Sets of acoustic tests were obtained with different geometries of the samples to achieve different stress-state histories at their critical point. There are four geometries, two cylindrical ones characterized as the flat and the slim, and two non-cylindrical ones, called the concave and the flange.

IBF has tested three temperatures (800°C, 900°C, 1000°C) and two strain rates (0.001 s-1, 0.0005 s-1). At least four samples from the surface of the slab have been tested for each combination and for each geometry to ensure statistically relevant results.

Macroscopic finite element simulations of the tests using constitutive law identified in Section 4.1 give the loading curve as well as the stresses, the strains and temperature histories in the region around the crack. Then these histories will be imposed as boundary conditions to the representative microscopic cell.

The acoustic data and the results of the representative cell simulations will be used, with the help of inverse modeling, to reach the parameters of the interface law.

7. First application

The growth of a crack for the simple model of Figure 10 has been simulated as a first application.

With this first example, the stability of the code when a crack is propagating has been analyzed. The parameters for the interface law are issued from [ONC 99]. For the continuous zone we simply used an elastic law with an elastic modulus of 32400 MPa which correspond to the elastic modulus of steel at 900°C.

The three pictures of Fig 11 illustrate the effect of the penalty coefficients k_s and k_n. In each of them, the stress σ_y in the direction perpendicular to the interface zone is represented. At this moment, no crack has appeared but voids are already growing in the interface. Figure 11a is a reference case with no interface element. Figure 11b, interface elements have been introduced, $k_s = k_n = 100000$ MPa/mm and in Figure 11c $k_s = k_n = 10000$ MPa/mm. The presence of interface elements introduces a softer zone in the mesh. Of course, this effect increases if the penalty coefficients decrease. For the small penalty coefficients, the perturbation is more important and introduces a stress concentration even when the interface is still in contact. The interface seems to be already open but this is only due to the penalty method, the cracking criterion has not yet been reached. In conclusion, we have to take the first values for

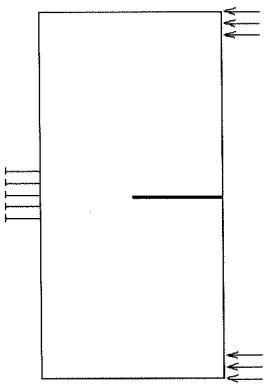

Figure 10. *Loads and fixations applied to the simple model. The arrows indicate the imposed displacements, the fixations are drawn on the left. The line in the middle represents the zone where interface elements have been put and where the crack can propagate. The size of the model is 1mm x 2mm.*

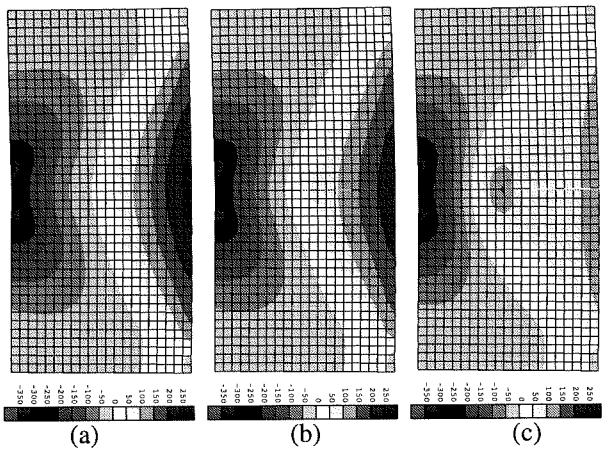

Figure 11. *Stress maps (σ_y) a) without interface elements, b) with interface elements $k_s = k_n = 100000$ MPa/mm, and c) $k_s = k_n = 10000$ MPa/mm.*

the penalty coefficients, keeping in mind, however, that too high coefficients could introduce convergence problems.

Figure 12 shows the evolution of the crack for $k_s = k_n = 100000$ MPa/mm. Picture a) is identical to the one presented in Figure 11b. In picture b), the crack has propagated on four elements. In picture c) the propagation extends on eight elements. In picture d), all the interface elements are opened. The stress concentrates around the crack tip and decreases in the right half of the specimen as the crack propagates.

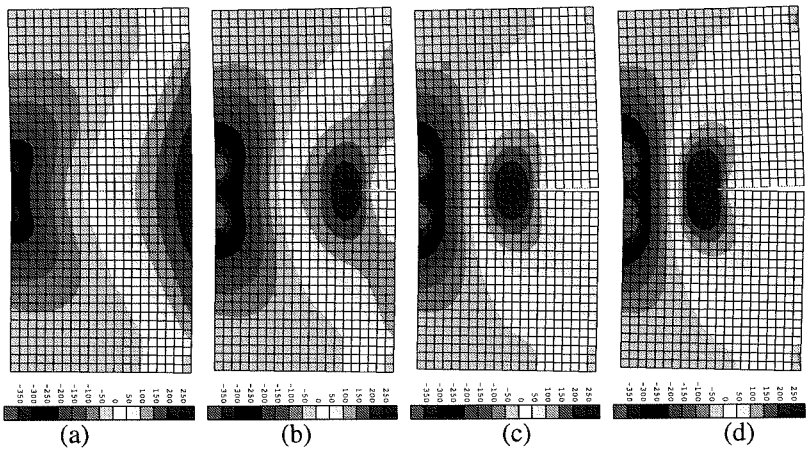

Figure 12. *Stress maps (σ_y) at different steps of the crack propagation in the course of a simulation.*

8. Conclusions

The research is dedicated to a microscopic study of damage at high temperature of micro-alloyed steel for continuous casting.

The development of the damage model is progressing in parallel with the analysis of the experimental tests.

The Norton-Hoff law has been identified and will be used in all the future simulations. Most of all, through the damage experimental study, we have already at our diposal a set of identification tests for the damage law as well as validation tests for this study.

We have succeeded in using our contact element to model crack propagation in a simple test and the results were very encouraging. The next step is to apply it to more complex cases.

Acknowledgements

S. Castagne and A.M. Habraken thank the National Fund for Scientific Research of Belgium (FNRS) for its support. Industrial partners ARCELOR and its research teams IRSID and the Technical Direction of Cockerill Sambre are acknowledged as well as IBF and CRM who performed experimental studies. The authors thank Prof. J. Lecomte-Beckers (ULg) for her help in the interpretation of the micro-graphic analysis.

9. References

[ASH 72] ASHBY M. F., "Boundary defects and atomistic aspects of boundary sliding and diffusional creep", *Surface Sci.*, vol. 31, 1972, p. 498-542.

[BUN 82] BUNGE H. J., *Texture Analysis in Materials Science*, Butterworths Publishers, London, 1982.

[CAS 01] CASTAGNE S., "Damage in continuous casting of steel: towards a microscopic representative cell", D.E.A. graduation work, University of Liège, 2001.

[COH 95] COHEUR J.-P., *Connaissance des matériaux métalliques*, University of Liège, 1995.

[GAM 01] GAMSJÄGER E., FISHER F. D., CHIMANI C. M., SVOBODA J., "Large strain concentration during continuous casting — a micromechanical study of the diffusional phase transformation", HABRAKEN A. M., Ed., *Proceedings of the 4th international ESAFORM conference on material forming*, Liège, 23-25 April 2001, University of Liège, p. 871-874.

[GIE 94] VAN DER GIESSEN E., TVERGAARD V., "Development of final creep failure in polycrystalline aggregates", *Acta Metall.*, vol. 42, 1994, Page 959.

[HAB 98] HABRAKEN A. M., CESCOTTO S., "Contact between deformable solids, the fully coupled approach", *Mathematical and Computer Modelling*, vol. 28, num. 4-8, 1998, p. 153-169.

[KOP 99] KOPP R., BERNARTH G., "The determination of formability for cold and hot forming conditions", *Steel Research*, vol. 70, num. 4+5, 1999, p. 147-153.

[LIU 94] LIU Y., KAGEYAMA Y., MURAKAMI S., "Creep fracture modeling by use of continuum damage variable based on Voronoi simulation of grain boundary cavity", *Int. J. Mech. Sci.*, vol. 40, num. 2-3, 1994, p. 765-795.

[ONC 99] ONCK P., VAN DER GIESSEN E., "Growth of an initially sharp crack by grain boundary cavitation", *J. Mech. Phys. Solids*, vol. 47, 1999, p. 99-139.

[PAS 00] PASCON F., "Finite element modelling of contact between the strand and the mould in continuous casting", D.E.A. graduation work, University of Liège, 2000.

[REM 01] REMY M., "OIMesh (alpha release) : Brief Status of the program and preliminary user's manual", technical report, Nov. 2001, University of Liège.

[TVE 84] TVERGAARD V., NEEDLEMAN V., "Analysis of the cup-cone fracture in a round tensile bar", *Acta Metall.*, vol. 32, 1984, p. 157-169.

[WOL 01] WOLSKE M., "Investigations to the formability of micro-alloyed steel", Final report for r&d project ix/3/2000, April 2001, IBF and MSM.

[ZHU 95] ZHU Y., CESCOTTO S., "Unified and mixed formulation of the 4-node quadrilateral elements by assumed strain method: Application to thermomechanical problems", *Int. Journal for Numerical Method in Engineering*, vol. 38, 1995, p. 685-716.